

Diagnosics of Coronary Stenoses

Analysis of Arterial Blood Pressure Signals and Mathematical Modeling

Natalya Kizilova

Kharkov National University, Svobody sq., 4, Kharkov, Ukraine

Keywords: Arterial Blood Pressure, Pulse Wave, Coronary Arteries, Stenosis, Mathematical Modelling, Pressure, Flow Signal Processing.

Abstract: Severity of the coronary stenoses and necessity of the percutaneous coronary intervention is usually estimated basing on analysis of the pressure and flow signals measured in vivo by a pressure gauge at certain distances before and after the stenosis. In the paper the differences in the pressure gradients at different stenosis severity are shown and discussed. A method of decomposition of the measured biosignals into the mean and oscillatory components is proposed. A mathematical model of the steady and pulsatile flow through the viscoelastic blood vessel in the presence of the rigid guiding wire is developed for biomechanical interpretation of the measured coronary blood pressure and flow signals. A novel approach for estimation the stenotic severity basing on the measured and computed data is proposed.

1 INTRODUCTION

Coronary artery disease, which is also known as atherosclerotic or ischemic heart disease, has become one of the most severe diseases causing a large number of deaths each year over the world. The partial occlusion of the stenosed artery and abnormal blood flow through it to the heart cells lead to insufficient oxygen delivery, especially when the possibilities of the perfusion regulation by the resistive coronary vessels are spent (Vlodaver et al, 2012). The causes to the formation of atherosclerotic lesions and arterial stenosis are still unknown but it is well established that the fluid dynamics, particularly the wall shear stress (WSS) and local pressure oscillations play an important role in the genesis of the disease (Layek et al, 2009).

In the absence of stenosis, the driving pressure gradient is constant over the coronary vessels. With progressing of the stenosis severity, the pressure gradient required to impel the blood through the narrowed path increases that results in a higher blood pressure at the inlet of the stenosed artery. The heart must work harder to increase the produced pressure, and when the blood supply to the working heart is insufficient the angina and even heart attack may occur. In-time diagnostics of the stenosed coronary arteries is crucial for timely therapy or/and surgery of the coronary lesions.

Coronary angiography (AG), intravascular ultrasound (IVUS) and coronary computed tomography angiography (CCTA) are commonly used for estimation of the stenosis severity by computations of the minimal lumen area (MLA) that is determined as the ratio of the minimal A_{\min} to normal A_0 lumen areas: $MLA = A_{\min}/A_0$ (%). The results of the AG, CCTA and IVUS-based MLA computations correspond well to each other (Caussin et al, 2006), but not in the case of the calcified wall (Li Y. and Zhanga, 2012). MLA gives geometric approximation of the stenosis and in many cases the stenoses with $MLA < 50\%$ remain insignificant and do not need stenting or bypass surgery, because sufficient perfusion is provided by autoregulation of the resistive vessels and collateral blood supply.

The functional severity of the stenosis can be estimated by the fractional flow reserve (FFR) defined as the ratio of the mean distal P_d and proximal (anterior) P_a coronary pressures measured via the pressure wire at certain distances before and after the stenosis during maximal hyperemia produced by intravenous adenosine administration that leads to relaxation of the myocardial vessels. The normal $FFR = 0.94 - 1.0$, whereas the $FFR < 0.75$ highly correlates with insufficient perfusion and myocardial ischemia. The patients from the grey zone $0.75 < FFR < 0.8$ may have had a risk of ischemia (Silber et al, 2005; Pijls, 2003). FFR reveals the

dangerous ischemia-producing lesions (Tonino, 2010), and it is recognized as gold standard for assessing the hemodynamic significance of coronary stenoses (Finn et al, 2012). The similar approach based on the flow velocities at rest and the hyperaemic state has also been developed.

Computational fluid dynamics (CFD) is widely used in advanced studies on the blood flows in rigid and compliant boundaries. The corresponding finite element and finite volume models and the computational schema have been used for the blood flow modeling in the vessels of different size up to the cellular level (Hinds et al, 2001). CFD study of the flow past symmetric and asymmetric stenoses in the straight, curved, helical and bifurcating tubes allow computations of the FFR values for every single stenosis as well as for the tandem, overlapping and bifurcational lesions. CFD approach allows virtual planning and estimation the outcomes of the surgery (stents, grafts, bypass) (Xiong, 2012), and the computed tomography (CT)-based virtual FFR estimation is a challenge that is widely discussed in recent publications (Taylor et al, 2013; Qi et al, 2013; Rajani et al, 2013). In the present paper some novel aspects of the FFR assessment and analysis of the measured pressure signals are proposed and discussed basing on the measurement data and the mathematical model of the blood flow in different rigid and compliant boundaries.

2 BLOOD PRESSURE SIGNALS

2.1 The Measurement Procedure

CFD computations and virtual FFR estimations are based on the 3D models of the viscous incompressible blood flow in the rigid patient-specific geometry of the larger epicardial coronary vessels recognized in AG and CCTA images, while the invasive FFR calculations are based on the *in vivo* measurements of the blood pressures before and after the stenosis at the presence of the guiding catheter and wire.

At local anesthesia, a guide catheter (Figure 1) is inserted into the orifice of the coronary artery through the femoral or radial artery. The pressure and flow signals in the coronary arteries can be measured by the pressure and Doppler guide wire (2). The diameters of the catheters can be chosen between $d=1.5-2.3$ mm, while the manufactured guidewires have the diameters $d=0.35-0.89$ mm.

According to the measurement data (Dodge, 1992), the main coronary arteries of adult humans

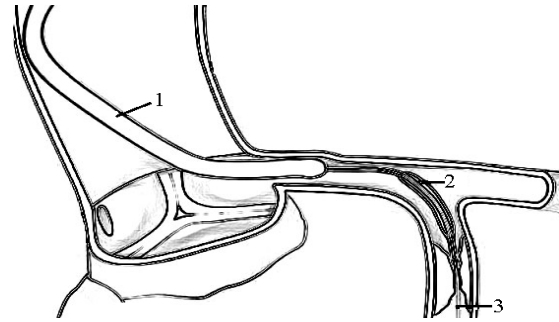


Figure 1: Schematic representation of the intravascular coronary examination: the guide catheter (1) in the coronary artery (2) and the guidewire with pressure and flow gauges (3) in the coronary stenosis (4).

have the following diameters: $d=4.5\pm 0.6$ mm for the left main artery; $d=3.7\pm 0.4$ mm and $d=1.9\pm 0.4$ mm for the proximal and distal parts of the left anterior descending artery; $d=3.4\pm 0.5$ mm for the left circumflex artery; $d=3.9\pm 0.6$ mm and $d=2.8\pm 0.5$ mm for the right coronary artery. The comparison of the diameters shows that both the catheter and wire can produce disturbances in the natural coronary blood flow and wave propagation.

In this study 45 data samples recorded in the epicardial coronary arteries of 32 patients with different stenosis severity diagnosed by the pressure gauge administrated via the guiding catheter have been analyzed. An example of the recorded data digitized from the CathLab software is presented in Figure 2. The red and green time-varying curves correspond to the pressure signals $P_a(t)$ and $P_d(t)$ accordingly, while the relatively smooth red and green lines correspond to their mean values. The measurements have been carried out during the adenosine administration which dynamics can be followed by the shift between the both oscillating and mean value curves. The FFR value indicated with yellow color has been computed automatically

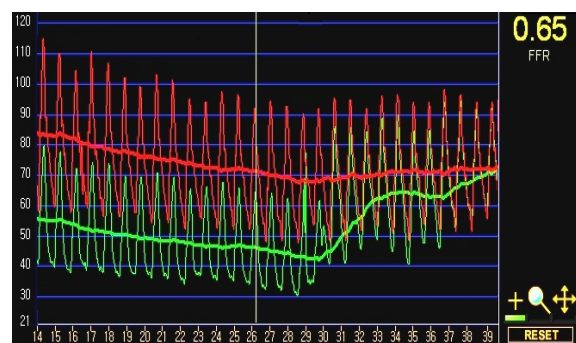


Figure 2: An example of the pressure signals recorded in the coronary artery by the pressure gauge and analyzed by the CathLab software.

by the CathLab software.

2.2 Smooth and Oscillatory Signals

Depending on the presence and severity of the stenosis, the pressure gradients in the signals measured before $P_a(t)$ and behind $P_d(t)$ the stenosis have significant differences. As the stenosis severity is progressing, the pressure behind the lesion drops first in diastole, while the pressure decrease after the peak systole is the same as in the pressure signal $P_a(t)$ (Fig.3a). Then the pressure drop in diastole becomes more significant (Fig.3b) and the differences in the pressure gradients appear also in the systole (Fig.3c).

The contour analysis of the $P_a(t)$ and $P_d(t)$ signals characterises their relative differences in slopes and values, while some novel information important for diagnostics can be driven from the $P_a(P_d)$, pressure-flow $P(U)$, and phase curves $P'(P)$ and $U'(U)$ computed from the measured signals where the stroke sign denotes the time derivative (Kizilova, 2013). For instance, the $P_a(P_d)$ curves computed from the $P_a(t)$ and $P_d(t)$ signals by elimination of time are presented by loops (Fig.4) slightly varying according to the heart rate, blood pressure and flow variability (Barclay et al, 2000; Trzeciakowski and Chilian, 2008). In spite of the heart rate and blood perfusion variability, the characteristic shape of the loop is preserved from beat to beat. When the myocardial perfusion is normal, the $P_a(P_d)$ loop is elongated and tends to the straight line (Fig.4a).

When the stenotic flow is critical in the term of the FFR values, the loop is shaped as digit '8' and the self-intersection point is located in the middle of the loop (Fig.4b). When the perfusion is insufficient, the FFR value is low and the urgent surgery is necessary, the $P_a(P_d)$ becomes 'thicker' and is looking as asymmetric '8' because of the asymmetric location of the self-intersection point (Fig.4c). Similar changes in the shapes of the dependencies $(P_a - P_d)$ on P_d and $(P_a - P_d)$ on P_a with progressing stenotic severity (functional, not geometrical!) have been observed in this study.

Representation of the measured blood pressure signals as cycles allows computation of different integral parameters like the area located inside the loop and its two subparts produced by the intersection point, variability of its location and slope.

The measured blood pressure signals $P_a(t)$ sometimes exhibit oscillating behaviour (Fig.5a), while in many cases they remain relatively smooth (Fig.3). Note that the $P_d(t)$ curves do not

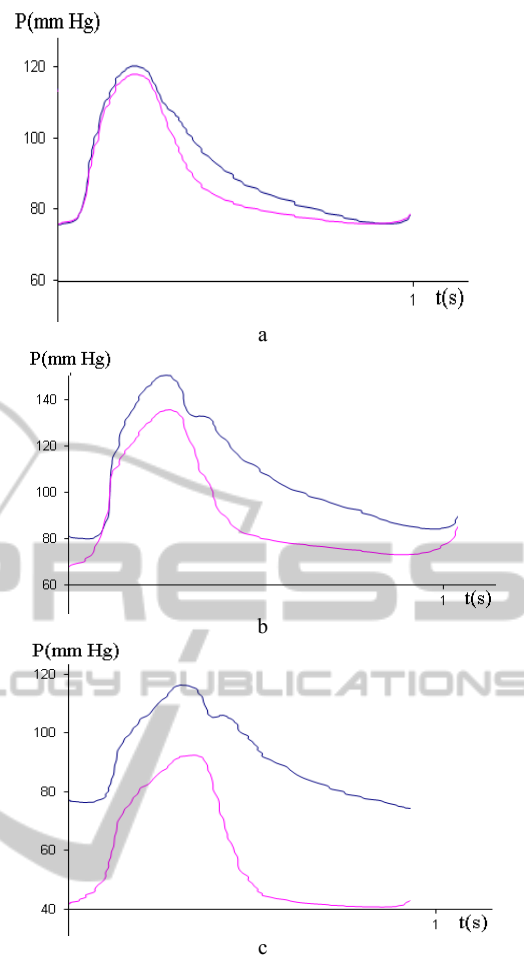


Figure 3: Blood pressure signals $P_a(t)$ (upper lines) and $P_d(t)$ (lower lines) measured in the epicardial coronary arteries with progressing stenosis severity (a,b,c).

demonstrate such oscillating behaviour, because the stenosis serves as the wave absorber producing reflected waves that propagate in the upstream direction and appear in the $P_a(t)$ signal. Similar regularity has been found in (Canic, 2006). Numerical simulations on the 1D model exhibit high-frequency, short wave-length reflected waves superimposed over the main wave front, and the computed high frequency oscillations were not a consequence of the numerical solver. Applying the 3–5 point smoothing filters or eliminating the high harmonics from the Fourier expansion, the $P_a(t)$ signals may be transformed in the smooth curves, but the computed FFR values will be always lower for the initial $P_a(t)$ (oscillatory) signals than for the smoother ones, because the smoothing procedure cuts the high oscillations and decreases the mean values of the signals. In that way the FFR computed on the oscillating curves can overestimate the

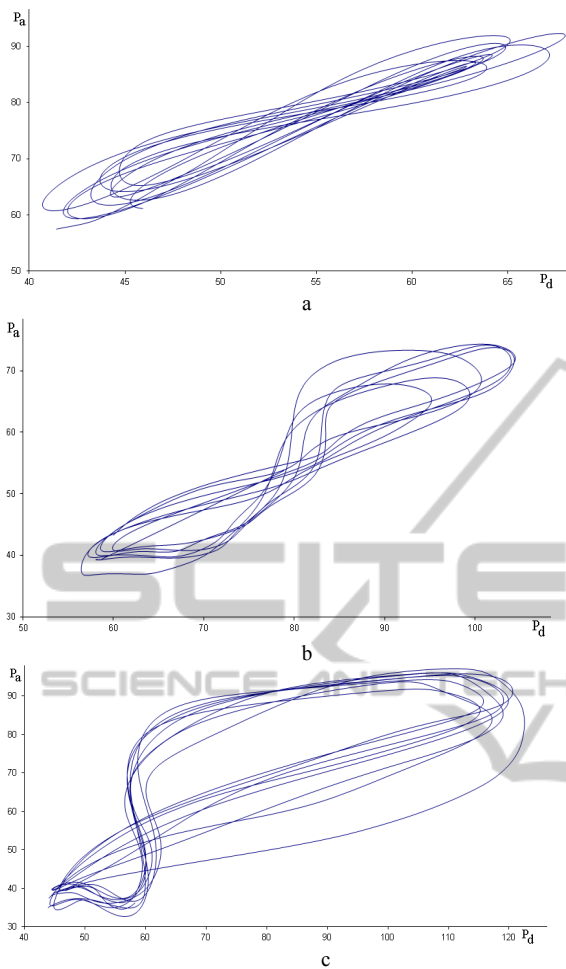


Figure 4: $P_a(P_d)$ loops for the stenotic flows at $FFR=0.86$ (a); $FFR=0.7$ (b); $FR=0.53$ (c).

stenosis severity. The smoothing leads to elimination of information that can be complementary to the FFR value and useful for more detailed diagnostics of the stenosis rigidity or presence of the atheroma, thrombus and fibrous cap. The $P_a(P_d)$ loops computed from the oscillating (Figure 6a) and smoothed (Figure 6b) pressure signals (see Figure 5a and 5b correspondingly) demonstrate the intensity of the high-frequency oscillations produced by additional wave reflection. The smoothed curves (Figure 5b) still can be classified and explained in correspondence to the examples presented in Figure 4, while the oscillating ones (Figure 5a) needs elaboration of new indexes and their biomechanical interpretation.

The pulsatile component of the measured pressure signals is not taken into account in the FFR computations, so decomposition of the signal $P(t)$ into the mean $\langle P(t) \rangle$ and oscillatory $P(t)$ terms and

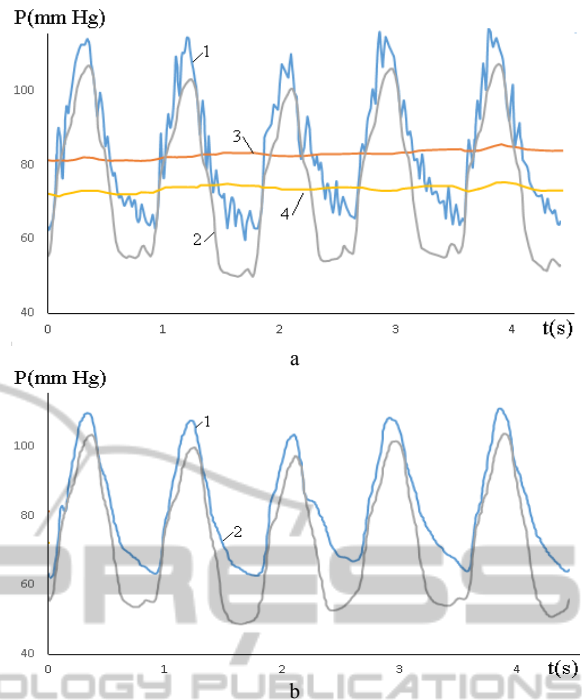


Figure 5: In vivo measured pressure curves before (a) and after (b) the smoothing procedure – $P_a(t)$ (1), $P_d(t)$ (2), $\langle P_a(t) \rangle$ (3), $\langle P_d(t) \rangle$ (4).

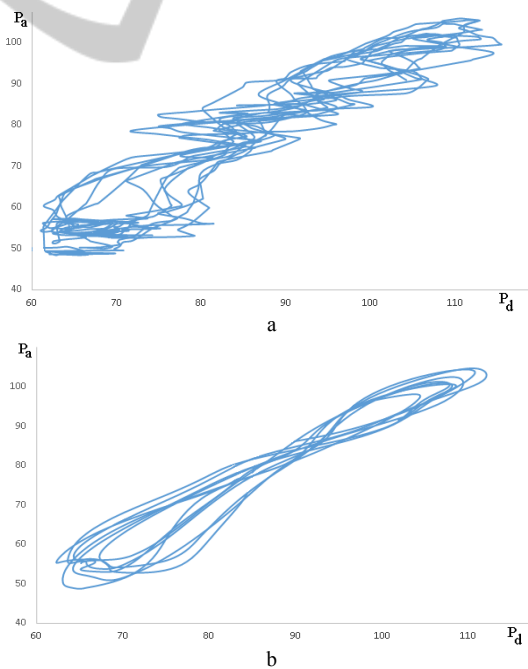


Figure 6: $P_a(P_d)$ loops for the oscillatory (a) and smoothed (b) pressure signals presented in Figures 5 a and 5b accordingly.

examination of the oscillatory component may be interested for the diagnostic purposes, as well as for

deeper understanding the blood flow and pressure wave propagation through the stenosis. For instance, the FFR values could be computed separately for the mean and oscillatory components as

$$\text{FFR} = \langle P_d(t) \rangle / \langle P_a(t) \rangle \quad \text{and} \quad \text{FFR}_{\text{osc}} = P_d(t) / P_a(t).$$

A comparative analysis of the FFR, FFR_{osc} and MLA values on a large representative group of the measurements in the stenosed arteries will be done in the next studies.

3 MATHEMATICAL MODEL

3.1 Steady Blood Flow between the Rigid Boundaries

The simplest model of the blood flow in the stenosed artery in the presence of the guide catheter (Fig.1) is the steady viscous flow between the rigid coaxial cylinders. According to the well-known solution of the problem the axial flow is

$$V(r) = \frac{\delta P}{4\mu L} \left(R_2^2 - r^2 + \frac{R_2^2 - R_1^2}{\ln(R_2/R_1)} \ln\left(\frac{r}{R_2}\right) \right) \quad (1)$$

where R_2 is the radius of the artery, R_1 is the radius of the wire/catheter, μ is the blood viscosity, L is the distance between locations of the proximal and distal measurement sites, δP is the measured pressure drop.

The virtual FFR in the straight part of the blood vessel is computed on the CFD model that in the limit of the rigid wall and the steady inflow tends to the Poiseuille solution

$$V_p(r) = \frac{\delta P}{4\mu L} (R_2^2 - r^2) \quad (2)$$

From (1) and (2) the error in the FFR values computed basing on the measurement signals and CFD computations can be estimated.

3.2 Pulsatile Blood Flow in Compliant Vessels

Heart contraction produces oscillations of the pressure and flow that propagate along the vessels, and the speed of the pulse waves vary from $c=5-8$ m/s in large elastic arteries to $c=10-12$ m/s in small resistive blood vessels. In elderly individuals and in the case of atherosclerosis, hypertension and some other cardiovascular disorders the pulse wave velocity increases up to $c=25$ m/s (Nichols et al, 2011). The wave propagation and reflection at the

arterial branching, atherosclerotic plaques, lesions and other non-uniformities produce complex superposition of the propagated and reflected waves. Spectral and wave-intensity analysis of the registered signals can reveal novel features of hemodynamics of stenosis and diagnostic indexes.

In this paper the axisymmetric wave propagation between the coaxial cylinders is proposed as the model of the pulsatile blood flow and pressure wave propagation in the compliant artery when the guiding catheter is inserted (Fig.1).

Fluid flow is governed by incompressible Navier-Stokes equations

$$\begin{aligned} \nabla \cdot \vec{v} &= 0, \\ \rho \left(\frac{\partial \vec{v}}{\partial t} + (\vec{v} \cdot \nabla) \vec{v} \right) &= -\nabla p + \mu \nabla^2 \vec{v}, \end{aligned} \quad (3)$$

the mass and momentum conservation equations for the incompressible vessel wall

$$\begin{aligned} \nabla \cdot \vec{u} &= 0, \\ \rho_w \frac{\partial^2 \vec{u}}{\partial t^2} &= -\nabla p_s + \nabla \cdot \hat{\sigma}, \end{aligned} \quad (4)$$

where \vec{v} is the flow velocity, \vec{u} is the wall displacement, ρ and ρ_w are the mass densities for the blood and wall, μ is the fluid viscosity, p and p_s are the hydrostatic pressures in the fluid and solid, $\hat{\sigma}$ is the stress tensor for the vessel wall.

The viscoelastic Kelvin-Voight body has been used as rheological model for the layers:

$$\sigma_i + \tau_w \frac{\partial}{\partial t} \sigma_i = A_{ik} \varepsilon_k + \mu_w \frac{\partial}{\partial t} \varepsilon_k \quad (5)$$

where A_{ik} is the matrix of elasticity coefficients, μ_w is the wall viscosity, τ_w is the stress relaxation time, $\vec{\sigma}^T = \{\sigma_{11}, \sigma_{22}, \sigma_{33}, \sigma_{23}, \sigma_{13}, \sigma_{12}\}$ is the stress vector, $\vec{\varepsilon}$ is similar strain vector, $\varepsilon_{ik} = (\nabla_i u_k + \nabla_k u_i) / 2$, T is transposition sign.

The boundary conditions include the no-slip flow condition at the inner rigid surface; continuity conditions for the fluid and solid velocities and the stress components at the fluid-wall interface:

$$r = R_1 : \vec{v} = 0 \quad (6)$$

$$r = R_2 : \vec{v} = \frac{d\vec{u}}{dt}, \quad \vec{\sigma}_n = \vec{\sigma}_n \quad (7)$$

At the outer surface of the blood vessel the no displacement or no stress boundary conditions can be taken in the form

$$r = R_2 + h : \bar{\sigma}_n = 0 \text{ or } \bar{u} = 0 \quad (8)$$

where h is the thickness of the arterial wall, n and τ denotes the normal and tangential components.

At the ends of the tube the fastening conditions for the tube

$$z = 0; L : \bar{u} = 0, \quad (9)$$

the input wave at the inlet and the wave reflection condition at the outlet of the tube

$$z = 0 : p(t, 0) = p_0(t), \quad (10)$$

$$z = L : p(t, L) = \Gamma p_0(t), \quad (11)$$

where Γ is the complex reflection coefficient equal to the ratio of the amplitudes of the reflected and propagates waves (Nichols et al, 2011), $\text{Re}(\Gamma) \in [0, 1]$ and $\text{Im}(\Gamma)$ corresponds to resistivity and capacity of the downstream vasculature (Lighthill, 2001) are considered.

The solutions of the problem (3) and problem (4)–(5) which are coupled via the boundary conditions (8)–(11) have been found as a superposition of the steady solution and small axisymmetric disturbance in the form of the normal mode:

$$\begin{aligned} \{\bar{v}, p\} &= \{\bar{v}^*, p^*\} + \{\bar{v}^\circ, p^\circ\} \cdot e^{st+ikz} \\ \{\bar{u}, p\} &= \{\bar{u}^*, p^*\} + \{\bar{u}^\circ, p^\circ\} \cdot e^{st+ikz} \end{aligned}$$

where \bar{v}° , \bar{u}° , p° , p_s° are the amplitudes of the corresponding disturbances, $k = k_r + ik_i$, $s = s_r + is_i$, s_i is the wave frequency, k_r is the wave number, s_r and k_i are spatial and temporal amplification rates, z is the axial coordinate. The steady part $\{\bar{v}^*, p^*\}$ is identified with Poiseuille flow (1) between the rigid surfaces.

The amplitudes \bar{v}° , \bar{u}° , p° , p_s° can be obtained from (3)–(4) as Fourier expansions

$$\begin{aligned} p &= \sum_{j=0}^n C_{1j} J_0(i\gamma_j r) e^{i(\omega_j t - \gamma_j x)}, \\ V_r &= \sum_{j=0}^n i\gamma_j (C_{2j} J_1(i\gamma_j r) + C_{3j} J_1(i\beta_j r) + \\ &\quad + C_{10j} K_0(i\gamma_j r) + C_{11j} K_0(\kappa_j r)) e^{i(\omega_j t - \gamma_j x)}, \\ V_x &= \sum_{j=0}^n i(C_{2j} \gamma_j J_1(i\gamma_j r) + C_{3j} \beta_j J_1(i\beta_j r) + \\ &\quad + C_{10j} K_0(i\gamma_j r) + C_{11j} K_0(\kappa_j r)) e^{i(\omega_j t - \gamma_j x)}, \end{aligned} \quad (12)$$

$$p_s = \sum_{j=0}^n (C_{8j} J_0(i\gamma_j r) + C_{9j} Y_0(i\gamma_j r)) e^{i(\omega_j t - \gamma_j x)},$$

$$\begin{aligned} U_r &= \sum_{j=0}^n i\gamma_j (C_{4j} J_1(\kappa_j r) + C_{5j} Y_1(\kappa_j r) + \\ &\quad + C_{6j} J_1(i\gamma_j r) + C_{7j} Y_1(i\gamma_j r) + \\ &\quad + C_{12j} K_1(i\gamma_j r) + C_{13j} K_1(\kappa_j r)) e^{i(\omega_j t - \gamma_j x)}, \end{aligned}$$

$$\begin{aligned} U_x &= \sum_{j=0}^n (C_{4j} \kappa_j J_0(\kappa_j r) + C_{5j} \kappa_j Y_0(\kappa_j r) + \\ &\quad + C_{6j} i\gamma_j J_0(i\gamma_j r) + C_{7j} i\gamma_j Y_0(i\gamma_j r) + \\ &\quad + C_{12j} K_0(i\gamma_j r) + C_{13j} K_0(\kappa_j r)) e^{i(\omega_j t - \gamma_j x)}. \end{aligned}$$

where $\beta_j^2 = \gamma_j^2 + i\omega_j/\nu$, $\kappa_j^2 = \omega_j^2 \rho_w / \mu_w - \gamma_j^2$, $\gamma_j = \omega_j / c_j$, c_j is the speed of the j -th harmonics, C_{kj} are unknown constants, $J_{0,1}$, $Y_{0,1}$ are Bessel and $K_{0,1}$ are modified Bessel functions of the 1st and 2nd kind.

The difference of the obtained solution (12) and the well-known Womersley solution at different boundary conditions (Cox, 1968; Milnor, 1989) is the modified Bessel functions $K_{0,1}$ in the expressions of the fluid velocities and wall displacements which become infinite at $r=0$ and, therefore, are absent in the Womersley solution for the hollow tube (at $R_1 \rightarrow 0$). The constants C_{kj} can be obtained by substitution of (12) into the boundary conditions (6)–(11). The resulting expressions are not present here because of their complexity.

4 RESULTS AND DISCUSSIONS

The pressure and flow distributions in the pulsatile flow between the coaxial rigid (guiding catheter/wire) and compliant viscoelastic surfaces have been computed on (9) using the following physiological parameters: $\rho=1050 \text{ kg/m}^3$, $\rho_s=1000\text{--}1300 \text{ kg/m}^3$, $\mu=3.5 \cdot 10^{-3} \text{ Pa}\cdot\text{s}$, $\mu_s=1 \text{ Pa}\cdot\text{s}$, $\tau_s=0.01\text{--}0.1 \text{ s}$, $R_1=0.18\text{--}1.25 \text{ mm}$, $R_2=0.75\text{--}2.5 \text{ mm}$, $\text{Re}(\Gamma)=0; 0.5; 0.9$, $\text{Im}(\Gamma)=1 \pm i$. The computed $p(t, r, x)$ and $\bar{v}(t, r, x)$ distributions have been averaged over the cross-sectional area between the two surfaces and then compared to the solutions of the same problem formulation (3)–(11) at $R_1=0$ (Lighthill, 2001). The aim of the study was to check whether the pressure signals measured for the pulsatile blood flow between two surfaces and in some cases in quite a narrow gap between them ($(R_2 - R_1)/R_2 \sim 0.5\text{--}0.75$) are consistent with the CFD

computations for the flows in rigid tubes without the axial obstacles (Taylor et al, 2013; Qi et al, 2013; Rajani et al, 2013). The input pressure waveforms $p_0(t)$ and the wave reflection coefficients Γ have been taken in the same form for both geometries.

The non-dimensional axial flow profiles $V_x(r^\circ)$ computed at the same pressure gradient $\delta P/L = \text{const}$ and different relative size of the guiding catheter/wire $R_1/R_2 = 0, 1 \div 0, 5$, where $r^\circ = r/R_2$ are presented in Figure 7. The flow profiles are built at $r \in [R_1/R_2, 1]$, non-dimensional by the maximal Poiseuille velocity, and the axial obstacle is plotted at $r = \pm 0.1$. The non-dimensional WSS at the inner and outer surfaces are presented in Figure 8. In the presence of the catheter/wire the total energy dissipation due to the viscous drag is bigger than in the hollow tube (Poiseuille flow). The dissipation is bigger for the thin wires located in the centre of the blood vessel in the region of the maximal blood velocity, because thinner wires produce bigger velocity gradients.

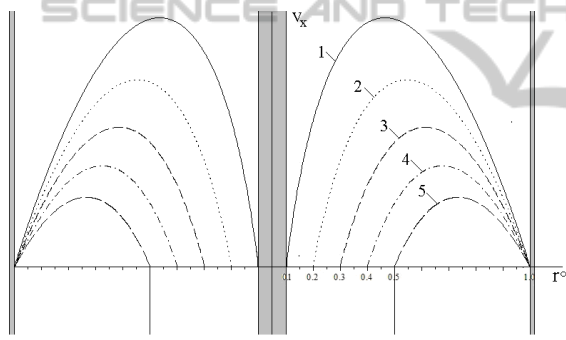


Figure 7: Axial flow profiles $V_x(r^\circ)$ at different values $R_1/R_2 = 0, 1; 0, 2; 0, 3; 0, 4; 0, 5$ (curves 1-5 accordingly).

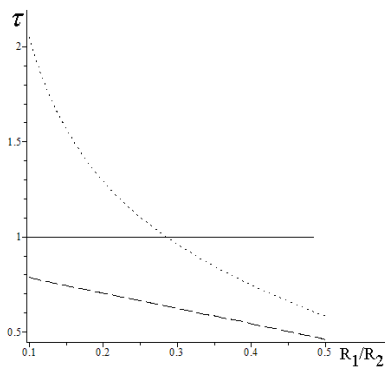


Figure 8: WSS at the inner rigid (dotted line) and outer compliant (dashed line) walls at $R_1/R_2 = 0, 1 \div 0, 5$. The solid line corresponds to the Poiseuille flow.

When the constant flow rate regime $Q = \text{const}$ between the cylinders is maintained by different

pressure gradients, the velocity profiles have different shapes produced by the main harmonics presented by the Bessel function $J_0(r)$ (Figure 9).

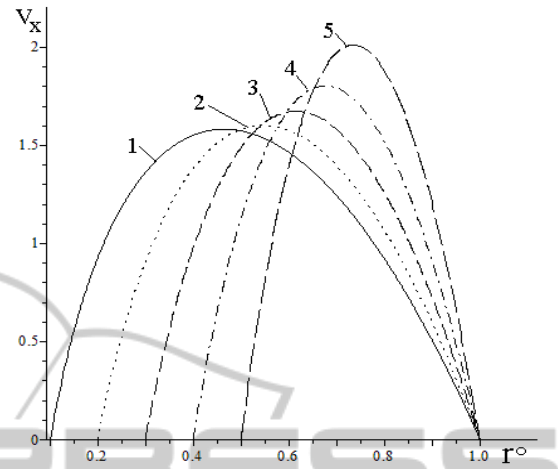


Figure 9: Axial flow profiles $V_x(r^\circ)$ for the case $Q = \text{const}$. The labels are the same as in Figure 7.

The FFR values have been computed for different sets of the material parameters and for the individual geometries of the 45 segments of the coronary arteries examined in this study (R_1, R_2, L, h). The corresponding distributions are shown in Figure 10.

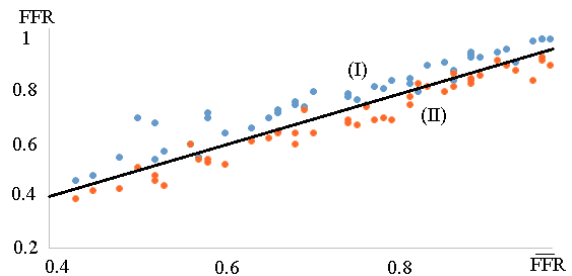


Figure 10: Measured FFR (vertical axis) versus the FFR computed on the standard (I) and developed (II) models.

In spite of possible patient-specific variations in some material parameters, the numerical computations on the developed model are closer to the FFR values measured via the CathLab, than the one computed for the flows in cylindrical geometries. Neglect of the high frequency components by smoothing of the measured signals leads to lower mean values for P_a but not P_d which results in overestimation of the stenosis severity. The obtained results must be also checked out on more complex geometries like curved/twisted tubes and in presence of smooth and irregular stenoses.

5 CONCLUSIONS

Pressure signals registered before $P_a(t)$ and behind $P_a(t)$ the stenosis possess different oscillatory behaviour, because of the wave reflections at the site of the stenosis. The important diagnostic parameters crucial for decision making on surgery of the stenosis (stenting, bypass, grafts) are made on the signals measured in the presence of the guiding catheter and wire with the pressure gauge, while the computational approaches for estimation of the hemodynamic parameters are based on the simplified models. It was shown the mathematical model of the pulsatile flow between the rigid and compliant cylinders is more precise for the virtual FFR estimation than the model of the flow in the hollow rigid tube without any obstacles along the axis.

It was shown the mathematical model of the steady and pulsatile flow between the rigid and compliant surfaces predicts more accurate results for the diagnostic index $\langle P_a(t) \rangle / \langle P_a(t) \rangle$. It was also shown the pulsatile high frequency component gives complementary information on the stenosis severity.

REFERENCES

- Barclay, K. D., Klassen, G. A., Young, Ch., 2000. A Method for Detecting Chaos in Canine Myocardial Microcirculatory Red Cell Flux. *Microcirculation*, 7(5): 335–346.
- Canic S., Hartley C. J., Rosenstrauch D., Tambaca J., Guidoboni G., Mikelic A., 2006. Blood flow in compliant arteries: an effective viscoelastic reduced model, numerics, and experimental validation. *Ann. Biomed. Engin.*, 34(4):575–592.
- Caussin, Ch., Larchez, Ch., Ghostine, S., et al, 2006. Comparison of Coronary Minimal Lumen Area Quantification by Sixty-Four-Slice Computed Tomography Versus Intravascular Ultrasound for Intermediate Stenosis. *Am. J. Cardiol.*, 98:871–876.
- Cox R. H., (1968). Wave propagation through a Newtonian fluid contained within a thick-walled, viscoelastic tube. *Biophys. J.*, 8:691-709.
- Dodge, J. T., Brown, B. G., Bolson, E. L., Dodge, H. T., 1992. Lumen diameter of normal human coronary arteries. Influence of age, sex, anatomic variation, and left ventricular hypertrophy or dilation. *Circulation*. 86:232–246.
- Fihn, S. D., Gardin, J. M., Abrams, J., et al, 2012. ACCF/AHA/ACP/AATS/PCNA/SCAI/STS guideline for the diagnosis and management of patients with stable ischemic heart disease. *Circulation*, 126:354–471.
- Hinds, M. T., Park, Y. J., Jones, S. A., Giddens, D. P., Alevriadou, B. R., 2001. Local hemodynamics affect monocytic cell adhesion to a three-dimensional flow model coated with E-selectin. *J. Biomech.* 34:95–103.
- Kizilova, N., 2013. Blood flow in arteries: regular and chaotic dynamics. In: Dynamical systems. Applications. /Awrejcewicz, J., Kazmierczak, M., Olejnik, P., Mrozowski, K. (eds). Lodz Politechnical University Press, 69–80.
- Layek, G. C., Mukhopadhyay, S., Gorla, R.S.R., 2009. Unsteady viscous flow with variable viscosity in a vascular tube with an overlapping constriction. *Intern. J. Engin. Sci.*, 47: 649–659.
- Li, Y., Zhanga, J., Lub, Z., Panb, J., 2012. Discrepant findings of computed tomography quantification of minimal lumen area of coronary artery stenosis: Correlation with intravascular ultrasound. *Europ. J. Radiol.*, 81:3270–3275.
- Lighthill, J., 2001. *Waves in Fluids*. Cambridge Univ. Press.
- Milnor W. R., (1989). *Hemodynamics*. Baltimore: Williams & Wilkins.
- Nichols, W., O'Rourke, M., Vlachopoulos, Ch. (eds.) *McDonald's Blood Flow in Arteries: Theoretical, Experimental and Clinical Principles*. 2011. 6th Edition.
- Pijls, N. H., 2003. Is it time to measure fractional flow reserve in all patients? *J. Am. Coll. Cardiol.*, 41:1122–1124.
- Qi X., Lv H., Zhou F., et al, 2013. A novel noninvasive method for measuring fractional flow reserve through three-dimensional modeling. *Arch. Med. Sci.*, 9(3):581–583.
- Rajani, R., Wang, Y., Uss, A., et al, 2013. Virtual fractional flow reserve by coronary computed tomography – hope or hype? *EuroIntervention*. 9(2):277–284.
- Silber, S., Albertsson, P., Aviles, F.F., et al., 2005. Guidelines for percutaneous coronary interventions. The Task Force for Percutaneous Coronary Interventions of the European Society of Cardiology. *Eur. Heart J.*, 26:804–847.
- Taylor, C. A., Fonte, T. A., Min, J. K., 2013. Computational fluid dynamics applied to cardiac computed tomography for noninvasive quantification of fractional flow reserve. *J. Am. Coll. Cardiol.*, 61: 2233–2241.
- Tonino, P. A. L., Fearon, W. F., De Bruyne, B. et al, 2010. Angiographic Versus Functional Severity of Coronary Artery Stenoses in the FAME Study Fractional Flow Reserve Versus Angiography in Multivessel Evaluation. *J. Am. Coll. Cardiol.*, 55:2816–2821.
- Trzeciakowski, J., Chilian, W., 2008. Chaotic behavior of the coronary circulation. *Med. & Biol. Eng. & Comp.*, 46(5): 433–442.
- Vlodaver Z., Wilson R.F., Garry D. J., 2012. *Coronary Heart Disease: Clinical, Pathological, Imaging, and Molecular Profiles*. Springer.
- Xiong G., Choi G., Taylor Ch. A., 2012. Virtual interventions for image-based blood flow computation. *Computer-Aided Design*, 44:3–14.